Inorganic Chemistry

pubs.acs.org/IC

Featured Article

# Direct Reduction of NO to $N_2O$ by a Mononuclear Nonheme Thiolate Ligated Iron(II) Complex via Formation of a Metastable $\{FeNO\}^7$ Complex

Aniruddha Dey, Therese Albert, Richard Y. Kong, Samantha N. MacMillan, Pierre Moënne-Loccoz,* Kyle M. Lancaster,* and David P. Goldberg*

Cite This: https://doi.org/10.1021/acs.inorgchem.2c02383

Read Online

ACCESS | Metrics & More | Article Recommendations | Supporting Information

**ABSTRACT:** Addition of NO to a nonheme dithiolate-ligated iron(II) complex, $Fe^{II}(Me_3TACN)(S_2SiMe_2)$ (**1**), results in the generation of $N_2O$. Low-temperature spectroscopic studies reveal a metastable six-coordinate $\{FeNO\}^7$ intermediate ($S$ = 3/2) that was trapped at −135 °C and was characterized by low-temperature UV−vis, resonance Raman, EPR, Mössbauer, XAS, and DFT studies. Thermal decay of the $\{FeNO\}^7$ species leads to the evolution of $N_2O$, providing a rare example of a mononuclear thiolate-ligated $\{FeNO\}^7$ that mediates NO reduction to $N_2O$ without the requirement of any exogenous electron or proton sources.

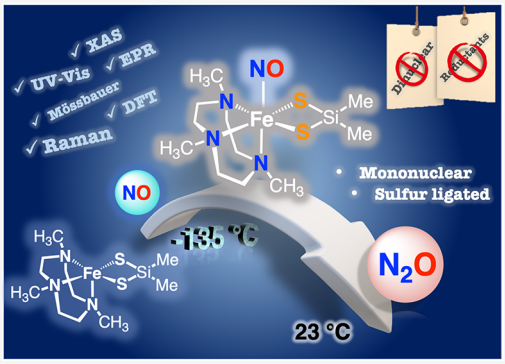


## INTRODUCTION

Thiolate ligation is known to play an important role in regulating the interaction of nitric oxide with metal cofactors in biology. The transport and storage of nitric oxide within cells is facilitated by iron−sulfur clusters which control the delivery of NO in the bloodstream and help in maintaining the physiological concentration of NO.[1−3] Certain enzymes are known to contain anionic thiolate donors that affect the binding affinity of NO. For example, nitrile hydratase (NHase) has sulfur ligands whose selective oxygenation controls the coordination of NO at the ferric active site.[4−6] The thiolate-ligated heme cofactor in cytochrome P450 is known to reduce NO to $N_2O$ and is the only enzymatic example of a mononuclear iron center that mediates the reduction of NO to $N_2O$.[7,8]

The reduction of NO to $N_2O$ is a crucial step in the denitrification pathway of the global nitrogen cycle.[9−12] This reductive transformation is carried out by nitric oxide reductase (NOR) in anaerobic pathogens, which catalyzes the $2e^-/2H^+$ reduction as shown in eq 1:[13]

$$2NO + 2e^- + 2H^+ \rightarrow N_2O + H_2O \quad (1)$$

Harmful microbes such as cyanobacteria, protozoa, and archaea use a special class of flavin-containing NORs, known as FDPnor, to combat the nitrosative stress generated by the immune response present in the bloodstream.[9,12,14−16] These enzymes are comprised of dinuclear iron centers, each with a five-coordinate environment around the metal centers and open sites for binding NO.[7,17] Although a number of mechanistic routes have been hypothesized for the reduction mechanism, the initial step in all of them involves the binding of NO to form a mononitrosyl $\{FeNO\}^7$ (Enemark−Feltham notation)[18] complex which undergoes a second nitrosylation to form a dinitrosyl $[\{FeNO\}^7]_2$ complex (Scheme 1). The $[\{FeNO\}^7]_2$ complex can accept reducing equivalents to form an $[\{FeNO\}^8]_2$ species, which results in $N_2O$ production. In an alternate scenario, the $[\{FeNO\}^7]_2$ complex can directly facilitate N−N bond formation to yield $N_2O$ without an additional reduction step. Although the two routes are equally probable during catalytic NO reduction by FDPnor, the successful production of $N_2O$ by the deflavinated FDPnor enzyme in a single turnover reflects the possibility that the metal centers can indeed act as electron reservoirs to sufficiently activate the FeNO unit and thereby nullify the requirement of any exogenous reductant.[19,20]

Significant efforts have been made to construct functional NOR models in order to examine the mechanism of biological NO reduction.[21−37] A few examples are known to reduce NO to $N_2O$ without the requirement of an added reductant.[31,38−41]

Received: July 7, 2022

**Scheme 1. $N_2O$ Formation Mediated by Nonheme Mononuclear Iron Nitrosyl Complexes: (A) Reduction of $\{FeNO\}^7$ to $\{FeNO\}^8$ to Form $N_2O$; (B) Structure of FDPnor and Direct $N_2O$ Formation from an $\{FeNO\}^7$ Complex; (C) This Work**

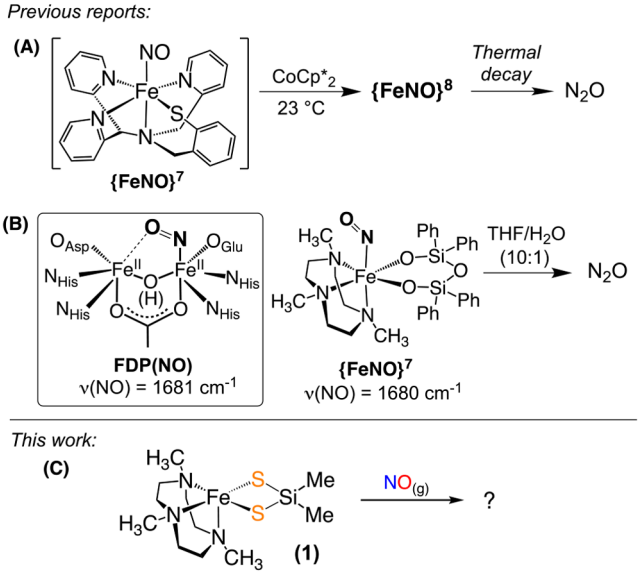


A diiron-dinitrosyl $[\{FeNO\}^7]_2$ complex was shown to produce $N_2O$ upon photoirradiation by white light, providing the first example of direct NO reduction to $N_2O$.[41] Another diiron(II) complex was reported to produce $N_2O$ directly upon exposure to NO, although no conformationally competent $\{FeNO\}^7$ species could be directly linked to the overall reduction reaction.[39] Multinuclear iron complexes have also been shown to carry out NO reduction in the absence of exogenous reductants.[31,38,40]

We have previously reported a structurally characterized $\{FeNO\}^7$ complex with the N3PyS ligand as a structural analogue for the NO-bound iron site in cysteine dioxygenase (CDO).[42−46] One-electron reduction of the $\{FeNO\}^7$ complex formed an $S = 1$ $\{FeNO\}^8$ complex, which led to the spontaneous production of $N_2O$ upon thermal decay. The N3PyS-ligated $\{FeNO\}^8$ complex was the first example of a mononuclear iron complex that produced $N_2O$.[47]

We recently reported a mononuclear $\{FeNO\}^7$ complex $Fe(NO)(Me_3TACN)((OSi^{Ph2})_2O)$,[48] and the nitrosyl stretching frequency ($\nu$(NO) = 1680 $cm^{-1}$) was found to be remarkably close to that known for FDPnor ($\nu$(NO) = 1681 $cm^{-1}$).[49] Formation of $N_2O$ was detected upon introduction of water to a THF solution of the complex. Such an observation motivated us to study the dependence of this reactivity upon the structural and electronic properties of the primary coordination sphere. Herein we report the reactivity of a silanedithiolate-ligated iron complex, $Fe^{II}(Me_3TACN)(S_2SiMe_2)$ (**1**),[50] with NO gas. The dianionic sulfur framework resulted in a new pattern of reactivity when compared to the previously reported dialkoxide $\{FeNO\}^7$ complex.[48] Complex **1** spontaneously evolves $N_2O$ upon being exposed to NO and does not require any additional reagent to cause $N_2O$ formation. In contrast to the widely observed stable nature of $\{FeNO\}^7$ complexes,[51] we observed a highly reactive metastable $\{FeNO\}^7$ species with the dithiolate ligand that could only be intercepted at −135 °C and characterized by low-temperature spectroscopic measurements. To the best of our knowledge, this is the first example of any thiolate-containing mononuclear $\{FeNO\}^7$ complex to directly produce $N_2O$ from NO without any added reductants.

## RESULTS AND DISCUSSION

**Reactivity with NO.** Complex **1** ($Fe^{II}(Me_3TACN)(S_2SiMe_2)$) is a nonheme high-spin ($S = 2$) mononuclear ferrous complex and is coordinated by three neutral nitrogen donors from the $Me_3TACN$ ligand and two anionic sulfur donors from the dithiolate ligand.[50,52] This environment results in an overall neutral, five-coordinated iron(II) complex with an open sixth coordination site. Addition of dry NO to a colorless solution of **1** in tetrahydrofuran (THF) results in the formation of a pale yellow solution with peaks at 500 and 618 nm in the UV−vis absorption spectrum. An analysis of the headspace of this reaction mixture after 5 min by gas chromatography (GC-ECD) showed evolution of $N_2O$ in 17% yield based on an assumed 2FeNO:1$N_2O$ reaction stoichiometry.[48] Switching to higher concentrations (∼2 mM) did not improve the $N_2O$ yield.

We hypothesized that the NOR activity exhibited by **1** proceeds through the formation of a transient mononitrosyl iron species that is unstable at room temperature. The addition of NO to **1** was carried out at low temperatures to allow a sufficient lifetime for any intermediates to be intercepted and characterized. Addition of NO to a precooled solution of **1** in 2-MeTHF at −135 °C results in a green color, indicating the formation of the new species **2** with UV−vis absorption peaks at 370 nm ($\varepsilon$ = 8750 $M^{-1}$ $cm^1$), 496 nm ($\varepsilon$ = 5000 $M^{-1}$ $cm^{-1}$), and 665 nm ($\varepsilon$ = 1875 $M^{-1}$ $cm^{-1}$) (Figure 1 and Scheme 2).

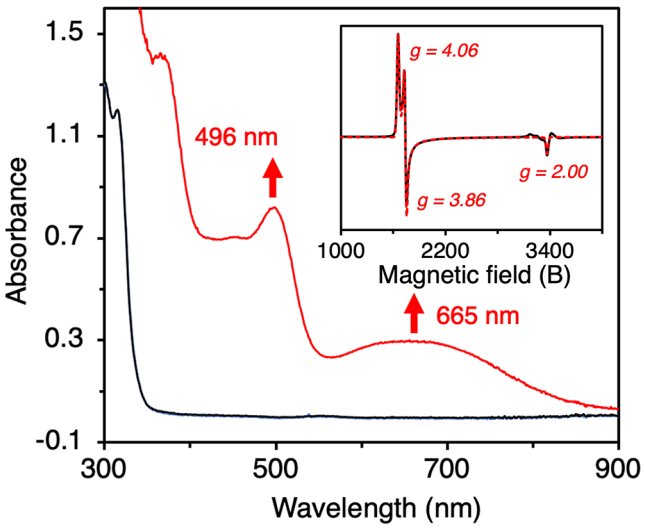


**Figure 1.** UV−vis spectra showing the conversion of **1** (black line) to **2** (red line) after NO addition in 2-MeTHF at −135 °C (0.8 mM). Inset: X-band EPR spectrum (black line) for **2** recorded at 22 K. The simulated spectrum is shown in red.

The new species **2** is stable for 1 h under inert conditions but starts to decay above −120 °C. The newly formed species is stable to vacuum/argon cycles and does not decay in the absence of excess NO in solution. A complete warmup of the reaction mixture produces the same UV−vis spectrum as was observed for NO addition to **1** under ambient conditions. Species **2** is highly reactive to trace amounts of air at low


https://doi.org/10.1021/acs.inorgchem.2c02383
Inorg. Chem. XXXX, XXX, XXX−XXX

**Scheme 2. Formation of the Mononuclear {FeNO}$^7$ Complex 2**

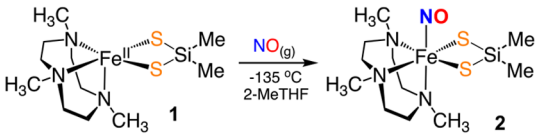


temperatures, and careful handling was required for further characterization.

The X-band EPR spectrum of a frozen sample of **2** in 2-MeTHF glass at 22 K revealed signals at $g$ = 4.06, 3.86, and 2.00 (Figure 1, inset). These values are within the range of high-spin $S$ = 3/2 {FeNO}$^7$ complexes. The ground spin state can be attributed to arise from the antiferromagnetic coupling between high-spin Fe(III) ($S$ = 5/2) and the NO$^-$ ($S$ = 1) ligand.[53,54] The EPR data for **2** are in contrast to those for our previously reported monothiolate ligated {FeNO}$^7$ complex [Fe(NO)(N3PyS)]BF$_4$, which showed a higher population of the $S$ = 1/2 spin state at 14 K.[46] The high-spin state ($S$ = 3/2) for **2** also contrasts with the five-coordinate, dithiolato {FeNO}$^7$ complex reported by Darensbourg, which exhibits an $S$ = 1/2 ground spin state.[55,56]

Analysis of the reaction mixture was followed by Mössbauer spectroscopy. We have previously reported the Mössbauer data for $^{57}$Fe-labeled $^{57}$**Fe-1**, which is comprised of a sharp doublet with the parameters $\delta$ = 0.90 mm s$^{-1}$ and $|\Delta E_Q|$ = 2.31 mm s$^{-1}$, and supports a high-spin state for the ferrous complex **1**.[50] The Mössbauer spectrum for **2** revealed a doublet with the parameters $\delta$ = 0.50 mm s$^{-1}$ and $|\Delta E_Q|$ = 1.08 mm s$^{-1}$ (Figure 2), which are in agreement with a mononuclear $S$ = 3/2 {FeNO}$^7$ center.[54] The spectrum also reveals a quantitative conversion of the ferrous species **1** to the {FeNO}$^7$ complex **2** at −135 °C. The asymmetric fit is reminiscent of the commonly observed vibrational anisotropy

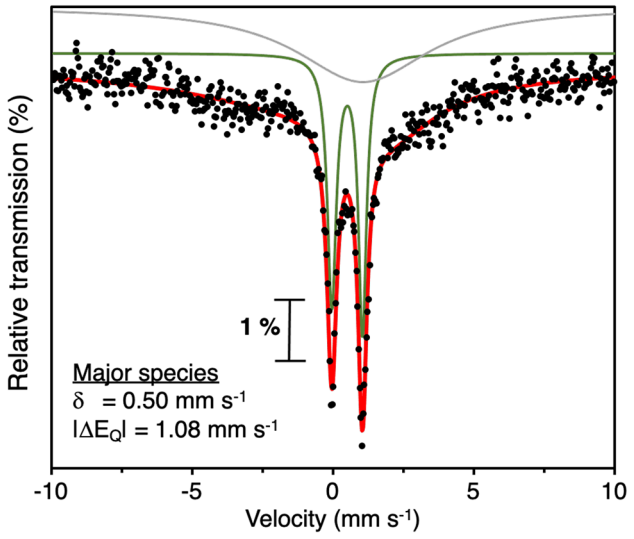


**Figure 2.** $^{57}$Fe-Mössbauer spectrum of a frozen solution of complex **2** in 2-MeTHF at 80 K: experimental data (filled circles); best fit (red line). The major subcomponent ($\delta$ = 0.50 mm s$^{-1}$, $|\Delta E_Q|$ = 1.08 mm s$^{-1}$ (90%)) is shown as a green line. A minor broad subcomponent ($\delta$ = 1.06 mm s$^{-1}$, $|\Delta E_Q|$ = 3.75 mm s$^{-1}$, $\Gamma_R = \Gamma_L$ = 5.7 (gray line)) was added to represent the intermediate relaxation of the doublet at 80 K.[48]

in low-symmetry complexes.[57−60] The isomer shift value is lower than that observed generally for $S$ = 3/2 [{FeNO}$^7$]$_x$ species, which typically fall in the range of 0.6−0.7 mm s$^{-1}$.[23,27,30,35,53]

Resonance Raman (RR) spectroscopy was used to analyze complex **2** for vibrations from the Fe−N−O unit. Excitation using a 514 nm laser line produced strong resonance enhancement at 479 cm$^{-1}$ that downshifted to 474 and 469 cm$^{-1}$ with $^{15}$NO and $^{15}$N$^{18}$O, respectively. This band can be assigned as the Fe−NO vibration and agrees well with an $S$ = 3/2 {FeNO}$^7$ complex that usually favors an Fe$^{III}$−NO$^-$ valence tautomer description.[53] An additional signal was observed at 953 cm$^{-1}$ that downshifts with $^{15}$NO and is assigned to a [$\nu$(Fe−NO) + $\delta$(Fe−N−O)] combination band, from which we can deduce the $\delta$(Fe−N−O) at 474 cm$^{-1}$ (Figure 3). No isotope-sensitive band could be detected in the

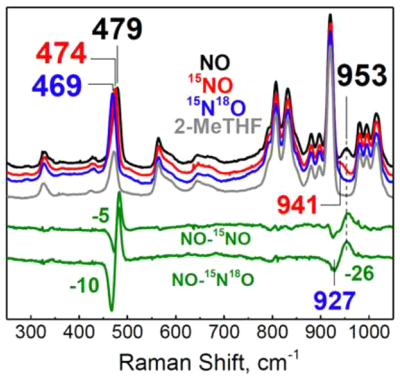


**Figure 3.** Low-temperature RR spectra of **2**-$^{14}$**NO** (black), **2**-$^{15}$**NO** (red), and **2**-$^{15}$**N**$^{18}$**O** (blue) in 2-MeTHF obtained with 514 nm laser excitation. The difference spectra are shown in green.

high-frequency region where N−O stretching vibrations are anticipated. Changing the excitation wavelength to 647, 488, and 407 nm did not improve the resonance enhancement conditions. This result is not unexpected, since most N−O stretching vibrations are at best weakly enhanced for $S$ = 3/2 {FeNO}$^7$ complexes. Indeed, detection of the $\nu$(N−O) modes by RR at low temperatures remain rare for synthetic models,[43,47,48,54] as well as for nonheme iron proteins.[49,61−63]

DFT calculations at the BP86/6-311g* level showed a distorted-octahedral structure with three nitrogen atoms, two sulfur atoms, and a nitrosyl moiety coordinated to the iron center (Figure 4). A single-point energy calculation at the B3LYP level of theory showed that the $S$ = 3/2 spin state for **2** was energetically more favored over the $S$ = 1/2 state (~1.03 eV), supporting the $S$ = 3/2 spin-state assignment for **2** as inferred from spectroscopic data (EPR, Mössbauer). The Fe−NO and N−O bonds were estimated to be at 1.71 and 1.19 Å, respectively. A geometry scan of the different orientations of the N−O bond along the $N_2S_2$ equatorial plane revealed a preferred orientation of the N−O bond toward the dithiolate ligand with an ∠Fe−N−O bond angle of 149°. The torsional potential increases significantly upon rotation of the N−O bond away from the dithiolate chelate and becomes the highest (increases by ~4 kcal mol$^{-1}$) when the N−O bond is oriented toward the TACN scaffold (Figure S5). Mössbauer calculations yielded the values of $\delta$ = 0.46 mm s$^{-1}$ and $|\Delta E_Q|$ = 1.59 mm s$^{-1}$ for the {FeNO}$^7$ complex **2**, which are in reasonable agreement with experiment.


https://doi.org/10.1021/acs.inorgchem.2c02383
Inorg. Chem. XXXX, XXX, XXX−XXX

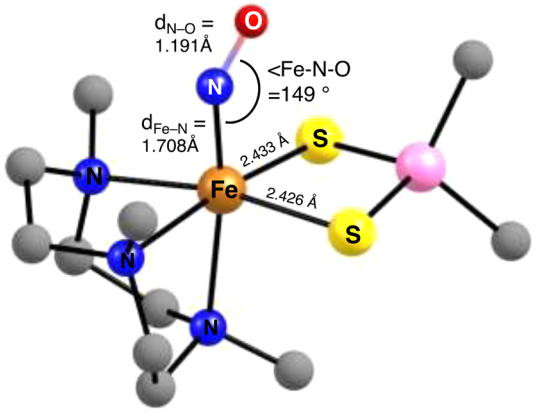


**Figure 4.** DFT-optimized structure of complex **2** in the $S$ = 3/2 spin ground state.

Time-dependent density functional theory (TD-DFT) calculations were performed with a THF continuum solvation approximation model. The majority of the electronic transitions arise from a ground state that is dominated by contributions from the ligand sulfur atoms. The major UV−vis peak at 496 nm can be attributed to a dipole-allowed electronic transition between the $NO_{\pi^*}$ ($\beta$-HOMO) and $\beta$-LUMO+4 $Fe^{III}(d_{x^2-y^2})$ orbitals (Figure 5). The high intensity of the 496 nm peak has an additional contribution from a $S(p_{x/y}) \rightarrow Fe^{III}(d_{x^2-y^2})$ transition with high oscillator strength. The broad absorbance centered at 665 nm is constituted by a combination of several excitations within the $\alpha/\beta$-spin manifolds. These excitations include ligand−ligand charge transfer transitions that occur from a S(thiolate) populated donor ($\alpha$-SOMO-1) to the $NO_{\pi^*}$ acceptor ($\alpha$-LUMO+1). A single-point energy calculation revealed that the unpaired spin density responsible for the $S$ = 3/2 ground spin state resides predominantly over the FeNO center.

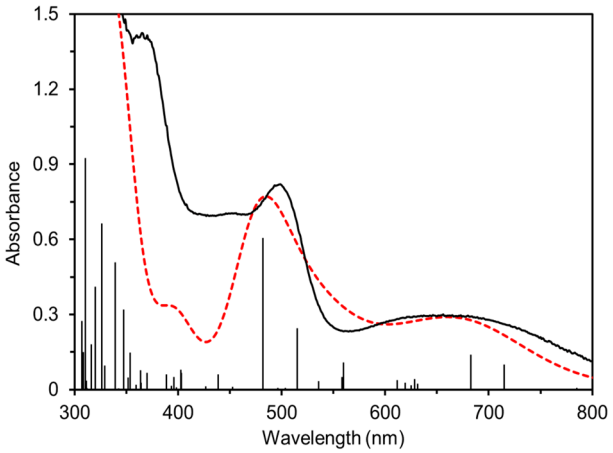


**Figure 5.** TD-DFT simulation (dashed red line) of the UV−vis absorption spectrum for **2** (solid black line). The computed spectral excitations are shown as vertical black bars underneath the data.

The poor resonance enhancement of the $\nu$(NO) vibration did not allow us to experimentally obtain the $\nu$(NO) stretching frequency. DFT calculations were employed to predict the $\nu$(NO) stretch for **2**. Frequency calculations for the gas-phase BP86 optimized geometry of **2** yielded a $\nu$(NO) stretch of 1659 $cm^{-1}$, which shifts to 1627 $cm^{-1}$ for the $^{15}N^{18}O$ isotopomer (Figure S6). The calculated NO vibrational stretch falls in the lower range of the NO vibration for $S$ = 3/2 $\{FeNO\}^7$ complexes[51] and supports the fact that species **2** contains a highly activated NO group.

The thermal instability of **2** precluded its structural characterization by crystallization techniques. We used Fe K-edge X-ray absorption spectroscopy to verify the structural integrity of complex **2** in solution. Fitting of the extended X-ray absorption fine structure (EXAFS) (Figure S7) revealed a six-coordinate environment around the metal center with three nitrogen scatterers at 2.28 Å and two sulfur scatterers at 2.47 Å, respectively (Figure 6). The Fe−NO scatterer was located at a distance of 1.76 Å and confirmed the presence of an intact nitrosyl-bound species in solution. The Fe−N(TACN), Fe−S, and Fe−NO bond lengths are all in good agreement with the optimized geometry in Figure 4.

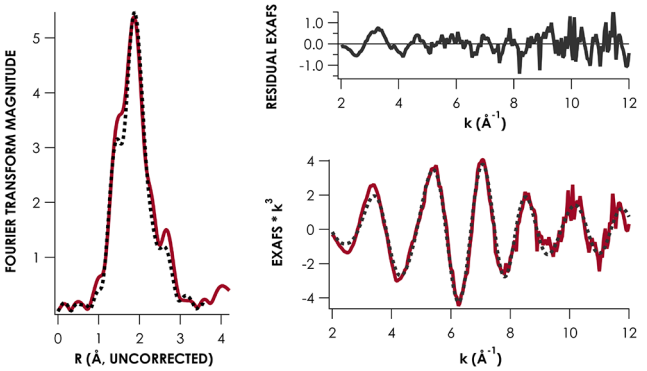


**Figure 6.** Fe K-edge EXAFS data and fit for **2**. Red traces correspond to the $k$-smoothed experimental data, while the dotted black lines represent a simulation of the data from the best fit (entry 4, Table S1 in the Supporting Information). Data were collected at 10 K and modeled in a window of $2 < k < 12$ $Å^{-1}$.

**Formation of $N_2O$.** Warming a solution of **2** in 2-MeTHF from −135 to 23 °C results in the disappearance of the green color associated with **2** and formation of a yellow solution. Analysis of the headspace by GC-ECD (Figure S3) showed the formation of $N_2O$ in 37% yield (2:1 FeNO:$N_2O$ ratio), which is higher than the $N_2O$ yield (17%) obtained from NO addition to **1** at room temperature (Scheme 3). This increase in the $N_2O$ yield correlates nicely with the $\{FeNO\}^7$ species being stabilized at low temperature, leading to effectively higher concentrations and more efficient $N_2O$ production. In contrast, the reaction of **1** with NO at room temperature may suffer from inefficient buildup of the $\{FeNO\}^7$ species caused by competing degradation pathways, resulting in lower yields of $N_2O$ product. The $N_2O$ yields for reactions run by warm-up

**Scheme 3. $N_2O$ Production via an $\{FeNO\}^7$ Complex**

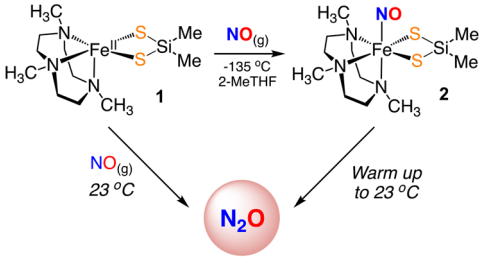



https://doi.org/10.1021/acs.inorgchem.2c02383
Inorg. Chem. XXXX, XXX, XXX−XXX

from −135 °C were not affected by replacing the excess NO(g) with the addition of a stoichiometric equivalent of NO (1 equiv per Fe, saturated NO(g) in 2-MeTHF stock solution, 1.1 mM). This observation indicates that excess NO is not required for $N_2O$ formation and suggests that free NO in solution is an unlikely participant in the mechanism of $N_2O$ formation. The disiloxide-ligated $\{FeNO\}^7$ analogue[48] of **2** releases $N_2O$ upon the addition of $H_2O$; however, addition of water to a solution of **2** in 2-MeTHF did not lead to any color change or increase in the $N_2O$ yield and indicated that **2** does not react with water. Similarly, weak proton donors (PhOH, $Et_3NH^+$) did not show any reactivity with **2**. Stronger acids resulted in the disappearance of the green color for **2** and formation of a colorless solution, suggesting complex decomposition.

Solutions of the $\{FeNO\}^7$ complex **2** following thermal equilibration to 23 °C showed absorbance features ($\lambda_{max}$ = 500, 618 nm) that are similar to those obtained upon the direct reaction of **1** with NO at 23 °C. A Mössbauer analysis revealed a mixture of products, with a major component (67%) consistent with a high-spin $Fe^{III}$ species and a minor component (32%) consistent with a high-spin $Fe^{II}$ species (Figure S4), but these species could not be characterized further.

Taken together, the data indicate that the sulfur-ligated $Fe^{II}$ complex **1** directly converts NO to $N_2O$ via formation of the $\{FeNO\}^7$ intermediate, **2**. This reaction does not require the addition of exogenous reductants to trigger $N_2O$ formation, in contrast to what is observed for the other $[\{FeNO\}^7]_x$ complexes,[23,27,30,35,47,64] with the exception of our earlier disiloxide analogue.[48,65]

## CONCLUSIONS

The reactivity of the mononuclear, sulfur-ligated $Fe^{II}$ complex **1** with dry NO gas was investigated. Addition of NO to **1** resulted in the spontaneous evolution of $N_2O$ at 23 °C. Carrying out the same reaction at −135 °C led to the formation of the metastable $\{FeNO\}^7$ complex **2**, which was characterized by UV−vis, resonance Raman, EPR, Mössbauer, XAS, and DFT studies. Complex **2** yields significant amounts of the NO reduction product $N_2O$ upon warming to 23 °C. The formation of $N_2O$ proceeds without the need for addition of an $H^+$ or $e^-$ source. Although the release of HNO from **2** could also lead to $N_2O$ production via disproportionation, we think production of HNO is unlikely, given the lack of influence of addition of $H^+$ to **2**. A speculative mechanism for $N_2O$ formation involves intramolecular ON−NO coupling on the metal, although we have no direct evidence for such a process at this time. The more polarizing nature and electron-donating tendency of the dithiolate ligand might be responsible for making the Fe−NO center more electron rich as compared to the dialkoxide-ligated complex, leading to a more reactive FeNO unit. These results bolster the hypothesis that has arisen from our previous work on NO activation by nonheme iron complexes:[47,48] a dinuclear iron complex is not required for the reduction of NO to $N_2O$ outside of a protein environment. This idea suggests that FeNO complexes can benefit from reactivity generated via simple solution-phase diffusion, whereas a protein needs to engineer a dinucleating site to sequester the reactive FeNO units in proximity to each other. The results presented here also indicate that substitution of the disiloxide ligation with the silanedithiolato donor in **1** significantly enhances the activation and reactivity of the subsequent $\{FeNO\}^7$ species toward NO to $N_2O$ reduction.

## EXPERIMENTAL SECTION

**General Considerations.** All syntheses and manipulations were conducted in an $N_2$-filled drybox (Vacuum Atmospheres, $O_2$ <0.2 ppm, $H_2O$ <0.5 ppm) or using standard Schlenk techniques under an atmosphere of Ar unless otherwise noted. $Me_3TACN$ was purchased from Matrix Scientific, degassed by three freeze−pump−thaw cycles, and stored over 3 Å molecular sieves prior to use. Hexamethylcyclotrisilathiane ($(Me_2SiS)_3$) and $Fe(OAc)_2$ were synthesized according to published procedures.[52,66] Isotopically enriched $^{57}Fe$ metal (95.5%) was purchased from Cambridge Isotope Laboratories (Andover, MA). Isotopically enriched $^{57}Fe(OAc)_2$ was synthesized according to a published procedure using $^{57}Fe$ powder.[67] All other reagents were purchased from commercial vendors and used without further purification. Tetrahydrofuran, pentane, hexane, and 2-MeTHF were dried over Na/benzophenone and subsequently distilled. Diethyl ether was obtained from a PureSolv solvent purification system. All solvents were degassed by a minimum of three freeze−pump−thaw cycles and stored over freshly activated 3 Å molecular sieves in the drybox following distillation. Nitric oxide gas was purchased from Matheson gases (Baltimore, MD), purified according to a literature procedure,[68] and stored in a dry, sealed Schlenk flask.

**Instrumentation.** The $^1H$ NMR spectra were measured on a Bruker 300 MHz or a Bruker 400 MHz spectrometer. UV−vis experiments were carried out on a Cary Bio-50 or Cary 60 UV−vis spectrophotometer equipped with a Unisoku USP-203A cryostat using a 1 cm modified Schlenk cuvette. EPR measurements were performed on a Bruker X-band EPR spectrometer in 4 or 5 mm quartz EPR tubes (Wilmad). Zero-field Mössbauer spectra were recorded on a spectrometer from SEE Co. (Edina, MN) operating in the constant-acceleration mode in a transmission geometry. Samples were cooled in an SVT-400 cryostat from Janis Research Co. (Wilmington, MA), using liquid $N_2$ as a cryogen for 80 K measurements. Isomer shifts were determined relative to the centroid of the spectrum of a metallic foil of $\alpha$-Fe collected at room temperature. Data analysis was performed using version F of the program WMOSS (www.wmoss.org), and quadrupole doublets were fit to Lorentzian line shapes.

**Preparation of 2 for EPR Spectroscopy.** A stock solution of **1** (3 mM, 2 mL) in 2-MeTHF was prepared. An aliquot (300 $\mu$L) of this solution was transferred to a 5 mm EPR tube and cooled to −130 °C in a pentane/$N_2$(l) bath. Excess NO was added, and the mixture was was shaken vigorously to result in a green solution. The EPR tube was annealed in $N_2$(l) and was stored at 80 K until data collection.

**Preparation of $^{57}Fe(NO)(Me_3TACN)(S_2SiMe_2)$ for Mössbauer Spectroscopy.** A solution of $^{57}Fe$-enriched **1**-$^{57}Fe$ (2.5 mM, 2 mL) in 2-MeTHF was transferred to a UV−vis cuvette, which was sealed and cooled to −135 °C. Excess NO was added to the solution and the mixture was stirred. Full formation of **2** was confirmed by monitoring of the UV−vis bands at 496 and 665 nm. The solution was poured into liquid nitrogen to yield green frozen pellets, which were crushed into a fine powder. An amount of the powder was loaded into a precooled Mössbauer cup and stored at 80 K until data collection. It should be noted that addition of NO directly into a Mössbauer sample cup containing a precooled solution (400 $\mu$L) of $^{57}$**Fe-1** in 2-MeTHF at −135 °C did not result in a uniform green coloration of the solution due to inhomogeneous mixing. The high viscosity of 2-MeTHF results in nonuniform mixing at low temperatures without adequate stirring.

**Preparation of 2 for Resonance Raman Spectroscopy.** A stock solution of the iron(II) complex was prepared by dissolving 8.0 mg (22.0 $\mu$mol) of crystalline **1** in 2-MeTHF (4.0 mL, 5.5 mM). An aliquot (200 $\mu$L) of this solution was transferred to an NMR tube and ∼1 mL of NO, $^{15}NO$, or $^{15}N^{18}O$ gas was added above the solution. The solution changed from colorless to green during a 2 min incubation, at which point the samples were frozen in liquid nitrogen and analyzed immediately.


https://doi.org/10.1021/acs.inorgchem.2c02383
Inorg. Chem. XXXX, XXX, XXX−XXX

Resonance Raman spectra were obtained on a custom McPherson 2061/207 spectrometer equipped with a liquid-nitrogen-cooled CCD detector (LN-1100 PB, Princeton Instrument). The 514 nm laser excitation was obtained from an argon laser (I90C-3, Coherent) and was focused on the samples maintained at 110 K inside a copper cold finger cooled with liquid nitrogen.

**Preparation of XAS Samples.** A solution of $^{57}$Fe-enriched **1-$^{57}$Fe** (13 mM, 2 mL) in 2-MeTHF was transferred to a cuvette, which was sealed and cooled to −135 °C. Excess NO was added, and the solution was stirred vigorously and monitored for full formation of the UV−vis bands at 496 and 665 nm. The solution was poured into liquid nitrogen to yield green frozen pellets, which were crushed into a fine powder. An amount of the powder was loaded into a precooled XAS sample cup. The slits were covered with 38 $\mu$m Kapton tape to make X-ray-transparent windows. Fe K-edge XAS data including extended X-ray absorption fine structure (EXAFS) data were obtained at the Stanford Synchrotron Radiation Lightsource (SSRL) at the 16-pole, 2 T wiggler beamline 9-3 under ring conditions of 3 GeV and 500 mA. A Si(220) double-crystal monochromator was used for energy selection. A Rh-coated mirror (set to an energy cutoff of 9 keV) was used for harmonic rejection, and the internal energy calibration was performed by assigning the first inflection point of an Fe-foil spectrum to 7111.2 eV upstream of the sample. Data were collected in fluorescence mode (windowed onto Fe K$\alpha$) using a Canberra 100-element Ge solid-state detector perpendicular to the incident beam. Elastic scatter into the detector was attenuated using a Soller slit. During collection, the sample was maintained at 10 K in an Oxford liquid He flow cryostat. Six scans were obtained and averaged. No evidence of photodamage was apparent from superimposing sequential scans. The scans were averaged and processed using the SIXPACK software package. A smooth pre-edge background was removed from each averaged spectrum by fitting a Gaussian to the pre-edge region and subtracting this polynomial from the entire spectrum. The postedge region was fit to a quadratic spline, flattened below 7130 eV, and then subtracted from the entire spectrum, and the data were normalized in the postedge absorption to 1.0. Coordinates for **2** were obtained from the DFT-optimized (BP86/def2-TZVP) structure and were used to generate models for scattering paths by FEFF6[69] as implemented in the Artemis module of Demeter 0.9.26.[70] Artemis was used to perform the fit, where floated parameters included the interatomic scattering distances ($R$), Debye−Waller factors ($\sigma^2$), and the energy shift ($\Delta E$). EXAFS were fit in the window of $2 < k' < 12$ for 1. Truncation before $k$ = 15 Å was dictated by a poor signal-to-noise ratio beyond $k$ = 12 Å.

**Preparation of Headspace GC Samples.** Headspace gas chromatography (GC) measurements were performed on an Agilent 8860 instrument equipped with a 1041 injector, electron capture detector, and molecular sieve capillary column. Grade 5.0 nitrogen was used as both the carrier (8 mL/min) and the makeup (22 mL/min) gas. For all measurements, the column oven temperature was kept constant at 150 °C. The temperatures of the injector oven and the detector oven were held at 200 and 300 °C, respectively. This GC method results in a characteristic retention time of 7.1 min for $N_2O$. The column also exhibits characteristic retention times for residual air from the syringe and NO at 1.6 and 1.9 min, respectively. Data analysis was performed with Openlab software. All samples for $N_2O$ detection were prepared under reduced-light conditions. The sample solutions (1 mL) were prepared inside Wheaton vials (6 mL) and incubated at 23 °C for 1 h in order to allow the complete partitioning of the $N_2O$ gas between the solution and the headspace. An aliquot of the headspace (60 $\mu$L) was withdrawn during each run by a gastight three-way syringe and injected into the GC. The yield of $N_2O$ was measured with respect to an $N_2O$ calibration curve, obtained with $N_2O$ generated via the base-mediated decomposition of Piloty's acid: $PhSO_2NHOH + KO^tBu \rightarrow 0.5N_2O + 0.5H_2O + PhSO_2^-K^+ + {}^tBuOH$. Details of the calibration curve can be found in ref 48.

**Computation Methods.** All calculations were performed in the ORCA-4.0.1.2 program package.[71] Fully relaxed geometry optimizations for the [Fe(NO)(Me$_3$TACN)(S$_2$SiMe$_2$)] complex (**2**) were carried out in the $S$ = 3/2 spin state using BP86 with the RI approximation and the D3BJ dispersion correction.[72,73] All optimizations utilized the CPCM solvation model for 2-methyltetrahydrofuran (dielectric constant 7.25; refractive index 1.407). Initial guess geometries were derived from the X-ray structure of [Fe$^{II}$(Me$_3$TACN)(S$_2$SiMe$_2$)] (**1**). To reduce computational cost, the 6-311g* basis set was implemented for the Fe, Si, S, N, and O atoms, while the less expensive 6-31g* basis set was implemented for the C and H atoms. The def2/J auxiliary basis set was applied to all atoms for the RI approximation. Numerical frequency calculations at the same level of theory confirmed that all optimizations had converged to true minima on the potential energy surface (i.e., no imaginary frequencies). Calculated IR spectra for **2-$^{14}$NO** and **2-$^{15}$NO** were plotted with 20 cm$^{-1}$ fwhm Gaussian broadening in ORCA (Figure S6). Band assignments were confirmed by inspection of the animated vibrational modes. Subsequently, single-point calculations were performed on the BP86-optimized geometries at the B3LYP level with a simulated 2-methyltetrahydrofuran dielectric constant. For the single-point energy calculation, the 6-311g* basis set was implemented for all atoms along with the def2/J auxiliary basis set for the RIJCOSX approximation. From the BP86-optimized geometries, $^{57}$Fe Mossbauer parameters were calculated using B3LYP with methanol solvation.[48] The CP(PPP) basis set was implemented for Fe, while the def2-TZVP basis set was applied to all remaining atoms.[74] Quadrupole splittings ($\Delta E_Q$) were obtained directly without any calibration or correction.

## ■ ASSOCIATED CONTENT

### Supporting Information

The Supporting Information is available free of charge at https://pubs.acs.org/doi/10.1021/acs.inorgchem.2c02383.

UV−vis, Mössbauer, EXAFS, and GC-ECD data and DFT coordinates (PDF)

## ■ AUTHOR INFORMATION


### Corresponding Authors

**David P. Goldberg** − *Department of Chemistry, The Johns Hopkins University, Baltimore, Maryland 21218, United States;* orcid.org/0000-0003-4645-1045; Email: dpg@jhu.edu

**Kyle M. Lancaster** − *Department of Chemistry and Chemical Biology, Cornell University, Ithaca, New York 14853, United States;* orcid.org/0000-0001-7296-128X; Email: kml236@cornell.edu

**Pierre Moënne-Loccoz** − *Department of Chemical Physiology and Biochemistry, Oregon Health & Science University, Portland, Oregon 97239, United States;* orcid.org/0000-0002-7684-7617; Email: moennelo@ohsu.edu

### Authors

**Aniruddha Dey** − *Department of Chemistry, The Johns Hopkins University, Baltimore, Maryland 21218, United States;* orcid.org/0000-0001-7162-0483

**Therese Albert** − *Department of Chemical Physiology and Biochemistry, Oregon Health & Science University, Portland, Oregon 97239, United States;* orcid.org/0000-0001-7248-0873

**Richard Y. Kong** − *Department of Chemistry and Chemical Biology, Cornell University, Ithaca, New York 14853, United States;* orcid.org/0000-0001-7891-9621

**Samantha N. MacMillan** − *Department of Chemistry and Chemical Biology, Cornell University, Ithaca, New York 14853, United States;* orcid.org/0000-0001-6516-1823

Complete contact information is available at: https://pubs.acs.org/10.1021/acs.inorgchem.2c02383




https://doi.org/10.1021/acs.inorgchem.2c02383
Inorg. Chem. XXXX, XXX, XXX−XXX

## Notes

The authors declare no competing financial interest.

## ■ ACKNOWLEDGMENTS

The NSF (CHE1955527 to D.P.G.) and the NIH (GM074785 to P.M.-L. and GM124908 to K.M.L.) are gratefully acknowledged for financial support. A.D. sincerely thanks Jessica Zarenkiewicz and Prof. J. P. Toscano (JHU Chemistry) for the use of GC instrumentation (headspace gas analysis). A.D. also thanks Jithin Thomas and Sudha Yadav for assistance with EPR. Use of the Stanford Synchrotron Radiation Lightsource, SLAC National Accelerator Laboratory, is supported by the U.S. Department of Energy, Office of Science, Office of Basic Energy Sciences, under Contract No. DE-AC02-76SF00515. The SSRL Structural Molecular Biology Program is supported by the DOE Office of Biological and Environmental Research and by the National Institutes of Health, National Institute of General Medical Sciences (P30GM133894).

## ■ REFERENCES

(1) Fitzpatrick, J.; Kim, E. Synthetic Modeling Chemistry of Iron-Sulfur Clusters in Nitric Oxide Signaling. *Acc. Chem. Res.* **2015**, *48*, 2453−2461.

(2) Johnson, D. C.; Dean, D. R.; Smith, A. D.; Johnson, M. K. Struucture, function, and formation of Biological iron-sulfur clusters. *Annu. Rev. Biochem.* **2005**, *74*, 247−281.

(3) Szaciłowski, K.; Chmura, A.; Stasicka, Z. Interplay between iron complexes, nitric oxide and sulfur ligands: Structure, (photo)reactivity and biological importance. *Coord. Chem. Rev.* **2005**, *249*, 2408−2436.

(4) Cheng, Z.; Xia, Y.; Zhou, Z. Recent Advances and Promises in Nitrile Hydratase: From Mechanism to Industrial Applications. *Front. Bioeng. Biotechnol.* **2020**, *8*, 1.

(5) Dey, A.; Chow, M.; Taniguchi, K.; Lugo-Mas, P.; Davin, S.; Maeda, M.; Kovacs, J. A.; Odaka, M.; Hodgson, K. O.; Hedman, B.; Solomon, E. I. Sulfur K-Edge XAS and DFT Calculations on Nitrile Hydratase: Geometric and Electronic Structure of the Non-heme Iron Active Site. *J. Am. Chem. Soc.* **2006**, *128*, 533−541.

(6) Nagashima, S.; Nakasako, M.; Dohmae, N.; Tsujimura, M.; Takio, K.; Odaka, M.; Yohda, M.; Kamiya, N.; Endo, I. Novel non-heme iron center of nitrile hydratase with a claw setting of oxygen atoms. *Nat. Struct. Mol. Biol.* **1998**, *5*, 347−351.

(7) Shoun, H.; Fushinobu, S.; Jiang, L.; Kim, S.-W.; Wakagi, T. Fungal denitrification and nitric oxide reductase cytochrome P450nor. *Philos. Trans R Soc. Lond B Biol. Sci.* **2012**, *367*, 1186−1194.

(8) Harris, D. L. Cytochrome P450nor: A nitric oxide reductase—Structure, spectra, and mechanism. *Int. J. Quantum Chem.* **2002**, *88*, 183−200.

(9) Ferousi, C.; Majer, S. H.; DiMucci, I. M.; Lancaster, K. M. Biological and Bioinspired Inorganic N-N Bond-Forming Reactions. *Chem. Rev.* **2020**, *120*, 5252−5307.

(10) Ford, C. L.; Park, Y. J.; Matson, E. M.; Gordon, Z.; Fout, A. R. A bioinspired iron catalyst for nitrate and perchlorate reduction. *Science* **2016**, *354*, 741−743.

(11) Matson, E. M.; Park, Y. J.; Fout, A. R. Facile Nitrite Reduction in a Non-heme Iron System: Formation of an Iron(III)-Oxo. *J. Am. Chem. Soc.* **2014**, *136*, 17398−17401.

(12) Wasser, I. M.; de Vries, S.; Moënne-Loccoz, P.; Schröder, I.; Karlin, K. D. Nitric Oxide in Biological Denitrification: Fe/Cu Metalloenzyme and Metal Complex $NO_x$ Redox Chemistry. *Chem. Rev.* **2002**, *102*, 1201−1234.

(13) Arikawa, Y.; Onishi, M. Reductive N-N coupling of NO molecules on transition metal complexes leading to $N_2O$. *Coord. Chem. Rev.* **2012**, *256*, 468−478.

(14) Romão, C. V.; Vicente, J. B.; Borges, P. T.; Frazão, C.; Teixeira, M. The dual function of flavodiiron proteins: oxygen and/or nitric oxide reductases. *J. Biol. Inorg. Chem.* **2016**, *21*, 39−52.

(15) Khatua, S.; Majumdar, A. Flavodiiron nitric oxide reductases: Recent developments in the mechanistic study and model chemistry for the catalytic reduction of NO. *J. Inorg. Biochem.* **2015**, *142*, 145−153.

(16) Tennyson, A. G.; Lippard, S. J. Generation, Translocation, and Action of Nitric Oxide in Living Systems. *Chem. Biol.* **2011**, *18*, 1211−1220.

(17) Kurtz, D. M., Jr. Flavo-diiron enzymes: nitric oxide or dioxygen reductases? *Dalton Trans.* **2007**, 4115−4121.

(18) Enemark, J. H.; Feltham, R. D. Principles of structure, bonding, and reactivity for metal nitrosyl complexes. *Coord. Chem. Rev.* **1974**, *13*, 339−406.

(19) Caranto, J. D.; Weitz, A.; Giri, N.; Hendrich, M. P.; Kurtz, D. M. A Diferrous-Dinitrosyl Intermediate in the $N_2O$-Generating Pathway of a Deflavinated Flavo-Diiron Protein. *Biochemistry* **2014**, *53*, 5631−5637.

(20) Hayashi, T.; Caranto, J. D.; Wampler, D. A.; Kurtz, D. M.; Moënne-Loccoz, P. Insights into the Nitric Oxide Reductase Mechanism of Flavodiiron Proteins from a Flavin-Free Enzyme. *Biochemistry* **2010**, *49*, 7040−7049.

(21) Cai, Z.; Tao, W.; Moore, C. E.; Zhang, S.; Wade, C. R. Direct NO Reduction by a Biomimetic Iron(II) Pyrazolate MOF. *Angew. Chem., Int. Ed. Engl.* **2021**, *60*, 21221−21225.

(22) Tao, W.; Bower, J. K.; Moore, C. E.; Zhang, S. Dicopper $\mu$-Oxo, $\mu$-Nitrosyl Complex from the Activation of NO or Nitrite at a Dicopper Center. *J. Am. Chem. Soc.* **2019**, *141*, 10159−10164.

(23) Jana, M.; White, C. J.; Pal, N.; Demeshko, S.; Cordes, C.; Meyer, F.; Lehnert, N.; Majumdar, A. Functional Models for the Mono- and Dinitrosyl Intermediates of FNORs: Semireduction versus Superreduction of NO. *J. Am. Chem. Soc.* **2020**, *142*, 6600−6616.

(24) Wijeratne, G. B.; Bhadra, M.; Siegler, M. A.; Karlin, K. D. Copper(I) Complex Mediated Nitric Oxide Reductive Coupling: Ligand Hydrogen Bonding Derived Proton Transfer Promotes $N_2O$(g) Release. *J. Am. Chem. Soc.* **2019**, *141*, 17962−17967.

(25) Kundu, S.; Phu, P. N.; Ghosh, P.; Kozimor, S. A.; Bertke, J. A.; Stieber, S. C. E.; Warren, T. H. Nitrosyl Linkage Isomers: NO Coupling to $N_2O$ at a Mononuclear Site. *J. Am. Chem. Soc.* **2019**, *141*, 1415−1419.

(26) Ferretti, E.; Dechert, S.; Demeshko, S.; Holthausen, M. C.; Meyer, F. Reductive Nitric Oxide Coupling at a Dinickel Core: Isolation of a Key *cis*-Hyponitrite Intermediate en route to $N_2O$ Formation. *Angew. Chem., Int. Ed. Engl.* **2019**, *58*, 1705−1709.

(27) White, C. J.; Speelman, A. L.; Kupper, C.; Demeshko, S.; Meyer, F.; Shanahan, J. P.; Alp, E. E.; Hu, M.; Zhao, J.; Lehnert, N. The Semireduced Mechanism for Nitric Oxide Reduction by Non-Heme Diiron Complexes: Modeling Flavodiiron Nitric Oxide Reductases. *J. Am. Chem. Soc.* **2018**, *140*, 2562−2574.

(28) Abucayon, E. G.; Khade, R. L.; Powell, D. R.; Zhang, Y.; Richter-Addo, G. B. Lewis Acid Activation of the Ferrous Heme-NO Fragment toward the N-N Coupling Reaction with NO To Generate $N_2O$. *J. Am. Chem. Soc.* **2018**, *140*, 4204−4207.

(29) Wijeratne, G. B.; Hematian, S.; Siegler, M. A.; Karlin, K. D. Copper(I)/NO(g) Reductive Coupling Producing a *trans*-Hyponitrite Bridged Dicopper(II) Complex: Redox Reversal Giving Copper(I)/$NO_{(g)}$ Disproportionation. *J. Am. Chem. Soc.* **2017**, *139*, 13276−13279.

(30) Jana, M.; Pal, N.; White, C. J.; Kupper, C.; Meyer, F.; Lehnert, N.; Majumdar, A. Functional Mononitrosyl Diiron(II) Complex Mediates the Reduction of NO to $N_2O$ with Relevance for Flavodiiron NO Reductases. *J. Am. Chem. Soc.* **2017**, *139*, 14380−14383.

(31) Wu, W.-Y.; Hsu, C.-N.; Hsieh, C.-H.; Chiou, T.-W.; Tsai, M.-L.; Chiang, M.-H.; Liaw, W.-F. NO-to-$[N_2O_2]^{2-}$-to-$N_2O$ Conversion Triggered by $\{Fe(NO)_2\}^{10}$-$\{Fe(NO)_2\}^9$ Dinuclear Dinitrosyl Iron Complex. *Inorg. Chem.* **2019**, *58*, 9586−9591.

(32) Kindermann, N.; Schober, A.; Demeshko, S.; Lehnert, N.; Meyer, F. Reductive Transformations of a Pyrazolate-Based Bioinspired Diiron-Dinitrosyl Complex. *Inorg. Chem.* **2016**, *55*, 11538−11550.



https://doi.org/10.1021/acs.inorgchem.2c02383
*Inorg. Chem.* XXXX, XXX, XXX−XXX

(33) Brozek, C. K.; Miller, J. T.; Stoian, S. A.; Dincă, M. NO Disproportionation at a Mononuclear Site-Isolated $Fe^{2+}$ Center in $Fe^{2+}$-MOF-5. *J. Am. Chem. Soc.* **2015**, *137*, 7495−7501.
(34) Berto, T. C.; Xu, N.; Lee, S. R.; McNeil, A. J.; Alp, E. E.; Zhao, J.; Richter-Addo, G. B.; Lehnert, N. Characterization of the Bridged Hyponitrite Complex $\{[Fe(OEP)]_2(\mu\text{-}N_2O_2)\}$: Reactivity of Hyponitrite Complexes and Biological Relevance. *Inorg. Chem.* **2014**, *53*, 6398−6414.
(35) Zheng, S.; Berto, T. C.; Dahl, E. W.; Hoffman, M. B.; Speelman, A. L.; Lehnert, N. The Functional Model Complex $[Fe_2(BPMP)(OPr)(NO)_2](BPh_4)_2$ Provides Insight into the Mechanism of Flavodiiron NO Reductases. *J. Am. Chem. Soc.* **2013**, *135*, 4902−4905.
(36) Wright, A. M.; Wu, G.; Hayton, T. W. Formation of $N_2O$ from a Nickel Nitrosyl: Isolation of the cis-$[N_2O_2]^{2-}$ Intermediate. *J. Am. Chem. Soc.* **2012**, *134*, 9930−9933.
(37) Xu, N.; Campbell, A. L. O.; Powell, D. R.; Khandogin, J.; Richter-Addo, G. B. A Stable Hyponitrite-Bridged Iron Porphyrin Complex. *J. Am. Chem. Soc.* **2009**, *131*, 2460−2461.
(38) Wu, W.-Y.; Tsai, M.-L.; Lai, Y.-A.; Hsieh, C.-H.; Liaw, W.-F. NO Reduction to $N_2O$ Triggered by a Dinuclear Dinitrosyl Iron Complex via the Associated Pathways of Hyponitrite Formation and NO Disproportionation. *Inorg. Chem.* **2021**, *60*, 15874−15889.
(39) Dong, H. T.; White, C. J.; Zhang, B.; Krebs, C.; Lehnert, N. Non-Heme Diiron Model Complexes Can Mediate Direct NO Reduction: Mechanistic Insight into Flavodiiron NO Reductases. *J. Am. Chem. Soc.* **2018**, *140*, 13429−13440.
(40) de Ruiter, G.; Thompson, N. B.; Lionetti, D.; Agapie, T. Nitric Oxide Activation by Distal Redox Modulation in Tetranuclear Iron Nitrosyl Complexes. *J. Am. Chem. Soc.* **2015**, *137*, 14094−14106.
(41) Jiang, Y.; Hayashi, T.; Matsumura, H.; Do, L. H.; Majumdar, A.; Lippard, S. J.; Moënne-Loccoz, P. Light-Induced $N_2O$ Production from a Non-heme Iron-Nitrosyl Dimer. *J. Am. Chem. Soc.* **2014**, *136*, 12524−12527.
(42) Confer, A. M.; Vilbert, A. C.; Dey, A.; Lancaster, K. M.; Goldberg, D. P. A Mononuclear, Nonheme $Fe^{II}$-Piloty's Acid ($PhSO_2NHOH$) Adduct: An Intermediate in the Production of $\{FeNO\}^{7/8}$ Complexes from Piloty's Acid. *J. Am. Chem. Soc.* **2019**, *141*, 7046−7055.
(43) Confer, A. M.; Sabuncu, S.; Siegler, M. A.; Moënne-Loccoz, P.; Goldberg, D. P. Mononuclear, Nonheme, High-Spin $\{FeNO\}^{7/8}$ Complexes Supported by a Sterically Encumbered $N_4S$-Thioether Ligand. *Inorg. Chem.* **2019**, *58*, 9576−9580.
(44) Dey, A.; Confer, A. M.; Vilbert, A. C.; Moënne-Loccoz, P.; Lancaster, K. M.; Goldberg, D. P. A Nonheme Sulfur-Ligated $\{FeNO\}^6$ Complex and Comparison with Redox-Interconvertible $\{FeNO\}^7$ and $\{FeNO\}^8$ Analogues. *Angew. Chem., Int. Ed.* **2018**, *57*, 13465−13469.
(45) McQuilken, A. C.; Matsumura, H.; Dürr, M.; Confer, A. M.; Sheckelton, J. P.; Siegler, M. A.; McQueen, T. M.; Ivanović-Burmazović, I.; Moënne-Loccoz, P.; Goldberg, D. P. Photoinitiated Reactivity of a Thiolate-Ligated, Spin-Crossover Nonheme $\{FeNO\}^7$ Complex with Dioxygen. *J. Am. Chem. Soc.* **2016**, *138*, 3107−3117.
(46) McQuilken, A. C.; Ha, Y.; Sutherlin, K. D.; Siegler, M. A.; Hodgson, K. O.; Hedman, B.; Solomon, E. I.; Jameson, G. N. L.; Goldberg, D. P. Preparation of Non-heme $\{FeNO\}^7$ Models of Cysteine Dioxygenase: Sulfur versus Nitrogen Ligation and Photorelease of Nitric Oxide. *J. Am. Chem. Soc.* **2013**, *135*, 14024−14027.
(47) Confer, A. M.; McQuilken, A. C.; Matsumura, H.; Moënne-Loccoz, P.; Goldberg, D. P. A Nonheme, High-Spin $\{FeNO\}^8$ Complex that Spontaneously Generates $N_2O$. *J. Am. Chem. Soc.* **2017**, *139*, 10621−10624.
(48) Dey, A.; Gordon, J. B.; Albert, T.; Sabuncu, S.; Siegler, M. A.; MacMillan, S. N.; Lancaster, K. M.; Moënne-Loccoz, P.; Goldberg, D. P. A Nonheme Mononuclear $\{FeNO\}^7$ Complex that Produces $N_2O$ in the Absence of an Exogenous Reductant. *Angew. Chem., Int. Ed.* **2021**, *60*, 21558−21564.
(49) Hayashi, T.; Caranto, J. D.; Matsumura, H.; Kurtz, D. M.; Moënne-Loccoz, P. Vibrational Analysis of Mononitrosyl Complexes in Hemerythrin and Flavodiiron Proteins: Relevance to Detoxifying NO Reductase. *J. Am. Chem. Soc.* **2012**, *134*, 6878−6884.
(50) Gordon, J. B.; Vilbert, A. C.; DiMucci, I. M.; MacMillan, S. N.; Lancaster, K. M.; Moënne-Loccoz, P.; Goldberg, D. P. Activation of Dioxygen by a Mononuclear Nonheme Iron Complex: Sequential Peroxo, Oxo, and Hydroxo Intermediates. *J. Am. Chem. Soc.* **2019**, *141*, 17533−17547.
(51) Van Stappen, C.; Lehnert, N. Mechanism of N-N Bond Formation by Transition Metal-Nitrosyl Complexes: Modeling Flavodiiron Nitric Oxide Reductases. *Inorg. Chem.* **2018**, *57*, 4252−4269.
(52) Komuro, T.; Matsuo, T.; Kawaguchi, H.; Tatsumi, K. Coordination Chemistry of Silanedithiolato Ligands Derived from Cyclotrisilathiane: Synthesis and Structures of Complexes of Iron(II), Cobalt(II), Palladium(II), Copper(I), and Silver(I). *Inorg. Chem.* **2003**, *42*, 5340−5347.
(53) Berto, T. C.; Speelman, A. L.; Zheng, S.; Lehnert, N. Mono- and dinuclear non-heme iron-nitrosyl complexes: Models for key intermediates in bacterial nitric oxide reductases. *Coord. Chem. Rev.* **2013**, *257*, 244−259.
(54) Brown, C. A.; Pavlosky, M. A.; Westre, T. E.; Zhang, Y.; Hedman, B.; Hodgson, K. O.; Solomon, E. I. Spectroscopic and Theoretical Description of the Electronic Structure of S = 3/2 Iron-Nitrosyl Complexes and Their Relation to $O_2$ Activation by Non-Heme Iron Enzyme Active Sites. *J. Am. Chem. Soc.* **1995**, *117*, 715−732.
(55) Sun, N.; Liu, L. V.; Dey, A.; Villar-Acevedo, G.; Kovacs, J. A.; Darensbourg, M. Y.; Hodgson, K. O.; Hedman, B.; Solomon, E. I. S K-Edge X-Ray Absorption Spectroscopy and Density Functional Theory Studies of High and Low Spin $\{FeNO\}^7$ Thiolate Complexes: Exchange Stabilization of Electron Delocalization in $\{FeNO\}^7$ and $\{FeO_2\}^8$. *Inorg. Chem.* **2011**, *50*, 427−436.
(56) Hess, J. L.; Conder, H. L.; Green, K. N.; Darensbourg, M. Y. Electronic Effects of (N2S2)M(NO) Complexes (M = Fe, Co) as Metallodithiolate Ligands. *Inorg. Chem.* **2008**, *47*, 2056−2063.
(57) Reguera, E.; Yee-Madeira, H.; Demeshko, S.; Eckold, G.; Jimenez-Gallegos, J. Nature of the Observed Asymmetry in Mössbauer Spectra of Iron (2+) Hexacyanometallates (III). *Z. Phys. Chem.* **2009**, *223*, 701−711.
(58) Kaczmarzyk, T.; Jackowski, T.; Dziliński, K.; Sinyakov, G. N. Asymmetry in Mössbauer spectra of $Fe^{III}$-azaporphyrin complexes. *Nukleonika* **2007**, *52*, S93−S98.
(59) McGrath, A. C.; Cashion, J. D. Gol'danskii-Karyagin effect and induced fields in rare earth-transition metal stannides. *Hyperfine Interact.* **2006**, *168*, 1103−1107.
(60) Varnek, V. A.; Lavrenova, L. G. Analysis of asymmetry of the Mössbauer bands of $Fe_xZn_{1-x}(4\text{-amino-}1,2,4\text{-Triazole})_3(NO_3)_2$ complexes with the spin transition $^1A_1 \rightleftarrows {}^5T_2$ proof of anisotropy of iron atom vibrations. *J. Struct. Chem.* **1995**, *36*, 97−103.
(61) Matsumura, H.; Chakraborty, S.; Reed, J.; Lu, Y.; Moënne-Loccoz, P. Effect of Outer-Sphere Side Chain Substitutions on the Fate of the *trans* Iron-Nitrosyl Dimer in Heme/Nonheme Engineered Myoglobins ($Fe_BMbs$): Insights into the Mechanism of Denitrifying NO Reductases. *Biochemistry* **2016**, *55*, 2091−2099.
(62) Matsumura, H.; Hayashi, T.; Chakraborty, S.; Lu, Y.; Moënne-Loccoz, P. The Production of Nitrous Oxide by the Heme/Nonheme Diiron Center of Engineered Myoglobins ($Fe_BMbs$) Proceeds through a *trans*-Iron-Nitrosyl Dimer. *J. Am. Chem. Soc.* **2014**, *136*, 2420−2431.
(63) Clay, M. D.; Cosper, C. A.; Jenney, F. E.; Adams, M. W. W.; Johnson, M. K. Nitric oxide binding at the mononuclear active site of reduced *Pyrococcus furiosus* superoxide reductase. *Proc. Natl. Acad. Sci. U.S.A.* **2003**, *100*, 3796−3801.
(64) Pal, N.; White, C. J.; Demeshko, S.; Meyer, F.; Lehnert, N.; Majumdar, A. A Monohydrosulfidodinitrosyldiiron Complex That Generates $N_2O$ as a Model for Flavodiiron Nitric Oxide Reductases: Reaction Mechanism and Electronic Structure. *Inorg. Chem.* **2021**, *60*, 15890−15900.


https://doi.org/10.1021/acs.inorgchem.2c02383
*Inorg. Chem.* XXXX, XXX, XXX−XXX

(65) Two other examples of $N_2O$ formation from $Fe^{II}$/NO have been reported, but no direct evidence for a competent $\{FeNO\}^7$ intermediate were noted. See refs 21 and 39.
(66) Catterick, J.; Thornton, P.; Fitzsimmons, B. W. Synthesis, magnetic properties, and Mössbauer spectra of polynuclear iron carboxylates. *J. Chem. Soc., Dalton Trans.* **1977**, 1420−1425.
(67) Weber, B.; Betz, R.; Bauer, W.; Schlamp, S. Crystal Structure of Iron(II) Acetate. *Z. Anorg. Allg. Chem.* **2011**, *637*, 102−107.
(68) Schopfer, M. P.; Mondal, B.; Lee, D.-H.; Sarjeant, A. A. N.; Karlin, K. D. Heme/$O_2$/•NO Nitric Oxide Dioxygenase (NOD) Reactivity: Phenolic Nitration via a Putative Heme-Peroxynitrite Intermediate. *J. Am. Chem. Soc.* **2009**, *131*, 11304−11305.
(69) Zabinsky, S. I.; Rehr, J. J.; Ankudinov, A.; Albers, R. C.; Eller, M. J. Multiple-scattering Calculations of x-ray-absorption spectra. *Phys. Rev. B* **1995**, *52*, 2995−3009.
(70) Ravel, B.; M, N. ATHENA, ARTEMIS, HEPHAESTUS: data analysis for X-ray absorption spectroscopy using IFEFFIT. *J. Synchrotron Radiat.* **2005**, *12*, 537−541.
(71) Neese, F. The ORCA program system. *WIREs Computational Molecular Science* **2012**, *2*, 73−78.
(72) Grimme, S.; Ehrlich, S.; Goerigk, L. Effect of the damping function in dispersion corrected density functional theory. *J. Comput. Chem.* **2011**, *32*, 1456−1465.
(73) Grimme, S.; Antony, J.; Ehrlich, S.; Krieg, H. A consistent and accurate ab initio parametrization of density functional dispersion correction (DFT-D) for the 94 elements H-Pu. *J. Chem. Phys.* **2010**, *132*, 154104.
(74) McWilliams, S. F.; Brennan-Wydra, E.; MacLeod, K. C.; Holland, P. L. Density Functional Calculations for Prediction of $^{57}Fe$ Mössbauer Isomer Shifts and Quadrupole Splittings in $\beta$-Diketiminate Complexes. *ACS Omega* **2017**, *2*, 2594−2606.


https://doi.org/10.1021/acs.inorgchem.2c02383
*Inorg. Chem.* XXXX, XXX, XXX−XXX